

Transmission probability through zigzag monolayer phosphorene superlattice

Atena boroughani (✉ atena_broghani@yahoo.com)

Iran University of Science and Technology

Edris Faizabadi

Iran University of Science and Technology

Hamed Hedayati

Iran University of Science and Technology

Research Article

Keywords: Transmission probability, Phosphorene, superlattice, barrier, transfer matrix

Posted Date: August 19th, 2021

DOI: <https://doi.org/10.21203/rs.3.rs-729566/v1>

License: © ⓘ This work is licensed under a Creative Commons Attribution 4.0 International License.

[Read Full License](#)

Transmission probability through zigzag monolayer phosphorene superlattice

A. Boroughani^{1,2}, E. Faizabadi², H.Hedayati²

¹Department of Physics, Hakim Sabzevari University, Sabzevar, Iran

²School of Physics, Iran University of Science and Technology, Tehran,
Iran

E-mail: atena_broghani@yahoo.com

E-mail: edris@iust.ac.ir

Abstract

The transportation of charge carriers for monolayer phosphorene superlattice has been investigated utilizing a transfer matrix method. Also, the efficacy of structural parameters has been studied on the transmission of charge carriers for the system. Our findings demonstrated that the barrier number at the superlattice structures performs an essential role in the transportation probability, that can be utilized in the design of nanoelectronic sets. Further, it can be comprehended that the transmission probability of one for the normal incident has occurred in twenty obstacles. On the other hand, the transmission probability of close to one has occurred in lower landing energies by increasing the obstacle number. As well, it has been understood the transmission probability of close to one by enhancing the barrier number can happen in barriers with a smaller width. According to the results, phosphorene can be used in the novel advances of two dimensional semiconductor devices in electronic applications.

Keywords: Transmission probability, Phosphorene, superlattice, barrier, transfer matrix

1.Introduction

Phosphorene is a 2D substance, with prominent properties such as the long relaxation time [1], high mobility of electron [2], anisotropy of carrier mobility[3–5], quasi-flat edge band [6], transport properties of magneto and Landau surfaces [7], and high optical capability[8]. Phosphorene arranged the honeycomb structure [9,10], that can be built at the laboratory[2,4–6,10,11]. Phosphorene is characterized through an anisotropic two bands k.p

[12], that is, congruent with the model of tight-binding [13]. The anisotropic structure of phosphorene's has created many theoretical calculations of phosphorene nanoribbons, prophesying extraordinary properties [15–29]. Black phosphorus has a direct optical gap between 1.3 to 1.7 eV that it can be decreased to 0.3 eV by increasing layer number. Thus, an energy range is obtained that is mainly utilizable for usages in the technologies of optoelectronic [29–32]. Theoretical computations also offer the presence of strongly bound exactions with connecting energy as large as 0.9 eV [32–35]. Phosphorus is one of the best 2D materials that, unlike graphene, is not limited to zero bandgaps & unlike silicene, it can be synthesized in substrates of metal [36–38]. In recent years, many studies have focused on the single phosphorene barrier, its structure, methods for its synthesis and, etc. So far, Zhenglu et al. have observed asymmetric tunneling of Klein for a single layer phosphorene [39]. Furthermore, Wu Qingyun et al. showed that unlike MoS₂ and graphene nanoribbons, the channels of carrier transport under the low bias are commonly placed in the internal of zigzag & armchair PNRs, as well as, being safe to the small number of edge defects. In addition, they made an apparatus of the PNR-based dual-gate field-efficacy transistor, with a high on/off ratio of 10³, which presented based on tuning effect of the electric field [16]. As well, Rahmani et al. showed that the properties of transport for nanoribbons of zigzag phosphorene is dependent on the location and number of the vacancies[40]. Here, we examine the transportation of Dirac fermions at the superlattice structures based on the nanostructure of phosphorene by transport matrix method. We illustrated that a full transmission probability at zero-landing angle occurred for twenty barriers. Also, our results show that by varying the width of a barrier, a full transmission probability in zero landing angle can occur at landing energies lower than obstacle height. As well, the results obtained for a single barrier are consonant with previous works that have been done by other researchers [1,39,41,42]. In the following, the transport matrix method and transmission probability calculation of Dirac fermions in phosphorene superlattice, have been described in section 2, and the numerical and theoretical results have been given in section 3. Eventually, the summary of results has been gathered in section 4.

2. Model and method

Here, the considered structure is a monolayer phosphorene which comprised N barriers of square ferromagnetic adjusted by a homogeneous field of electric, as shown in shape 1. In addition, the anisotropic effect of Rashba in phosphorene is not considered because it is in the

order of a few μeV for an utilized electric field of the order $10 \text{ meV}\text{\AA}^{-1}$ [43]. The Hamiltonian for the system at a tight-binding model can be written as following [43]:

$$\hat{H}_0(\mathbf{k}) = \begin{pmatrix} u_0 + \eta_x k_x^2 + \eta_y k_y^2 & \delta + \gamma_x k_x^2 + \gamma_y k_y^2 + i\chi k_y \\ \delta + \gamma_x k_x^2 + \gamma_y k_y^2 - i\chi k_y & u_0 + \eta_x k_x^2 + \eta_y k_y^2 \end{pmatrix} \quad (1)$$

Where $u_0 = -0.42\text{eV}$, $\eta_y = 0.58\text{eV}\cdot\text{\AA}^2$, $\eta_x = 1.01\text{eV}\cdot\text{\AA}^2$, $\delta = 0.76\text{eV}$, $\chi = 5.25\text{eV}\cdot\text{\AA}$, $\gamma_y = 3.93\text{eV}\cdot\text{\AA}^2$ and $\gamma_x = 3.83\text{eV}\cdot\text{\AA}$ are gained from the computations of the tight-binding model [44]. The potential of x-direction is defined as follow;

$$V'(x) = \begin{cases} V_0 & \text{for barrier areas} \\ 0 & \text{elsewhere} \end{cases} \quad (2)$$

That V_0 is a potential of the electronic that is regulated by the gate of metallic. As well, the efficacy of strip edges is not considered in this paper. Furthermore, the system is surveyed in the lack of phonon interactions for zero temperature. To solve equation $H\Psi = E\Psi$, it is surmised that incoming electrons with the angle of φ and spin s come from the left barrier (x-direction). Eigenvalues of energy and eigen functions for Hamiltonian can be obtained as follow:

$$E = u_0 + \eta_x k_x^2 + \eta_y k_y^2 \pm \lambda \sqrt{\chi^2 k_x^2 + [\delta + \gamma_x k_x^2 + \gamma_y k_y^2]^2} \quad (3)$$

$$\Psi = \frac{1}{\sqrt{2}} \begin{pmatrix} 1 \\ \lambda e^{-i\theta_k} \end{pmatrix} \quad (4)$$

Where $\lambda = \pm 1$ and θ_k is defined as:

$$\theta_k = \tan^{-1}(2\chi k_x / \delta + \gamma_x k_x^2 + \gamma_y k_y^2)$$

The functions of wave in the outer and inside regions are as follows [45–48];

$$\Psi(x,y) = \begin{cases} \frac{a}{\sqrt{2}} \begin{pmatrix} 1 \\ \lambda e^{-i\theta_k} \end{pmatrix} e^{i(k_x x + k_y y)} + \frac{b}{\sqrt{2}} \begin{pmatrix} 1 \\ -\lambda e^{i\theta_k} \end{pmatrix} e^{-i(k_x x - k_y y)} & \text{for the outside barrier areas} \\ \frac{c}{\sqrt{2}} \begin{pmatrix} 1 \\ \lambda' e^{-i\theta_q} \end{pmatrix} e^{i(q_x x + q_y y)} + \frac{d}{\sqrt{2}} \begin{pmatrix} 1 \\ -\lambda' e^{i\theta_q} \end{pmatrix} e^{-i(q_x x - q_y y)} & \text{for the inside barrier areas} \end{cases} \quad (5)$$

Where $\lambda' = \pm 1$ and θ_q is defined as:

$$\theta_q = \tan^{-1}(2\chi q_x / \delta + \gamma_x q_x^2 + \gamma_y q_y^2)$$

Here, c and a are transmission rates for the inside and outside obstacle regions, respectively, and d and b are reflection rates at the inside and outside barrier areas, respectively. Further,

k_x , k_y , q_x , and q_y are wave vectors along the x and y-direction in outer and inside obstacle regions, respectively, so they can be contained as follow:

$$k_x = k_f \cos \theta_k$$

$$k_y = k_f \sin \theta_k$$

Here

$$k_f = \frac{\sqrt{-b'' \pm \sqrt{b''^2 - 4a''c''}}}{\sqrt{2a''}}$$

where,

$$a'' = (\eta_x \cos^2 \varphi + \eta_y \sin^2 \varphi)^2 - (\gamma_x \cos^2 \varphi + \gamma_y \sin^2 \varphi)^2$$

and

$$b'' = -2(E - u_0)(\eta_x \cos^2 \varphi + \eta_y \sin^2 \varphi) - \chi^2 \cos^2 \varphi - 2\delta(\gamma_x \cos^2 \varphi + \gamma_y \sin^2 \varphi)$$

and

$$c'' = (E - u_0)^2 - \delta^2$$

and

$$q_x = \sqrt{\frac{(2\varepsilon\eta_x + f) \pm \sqrt{(2\varepsilon\eta_x + f)^2 - 4(\varepsilon^2 - D^2)(\eta_x^2 - \gamma_x^2)}}{2(\eta_x^2 - \gamma_x^2)}}$$

here,

$$\varepsilon = (E - V_0 - u_0 - \eta_y k_y^2)$$

$$f = 2D\gamma_x + \chi^2$$

$$D = (\delta + \gamma_y k_y^2)$$

The vector of wave endures constant along the y-direction so that $k_y = q_y$ because the structure in the y-direction is homogeneous [49]. The reflection ($r_{s's}$) and transmission ($t_{s's}$) can be calculated from the transfer matrix method by using the continuity in the functions of

a wave for the boundaries. The probability of transmission and reflection ($T_{s's}$ and $R_{s's}$) can be obtained by $T_{s's} = |t_{s's}|^2$ and $R_{s's} = |r_{s's}|^2$, respectively. Ultimately, the polarization of spin for phosphorene superlattice at zero temperature can be calculated as follow:

$$SP = \frac{T_{\uparrow} - T_{\downarrow}}{T_{\uparrow} + T_{\downarrow}} \quad (6)$$

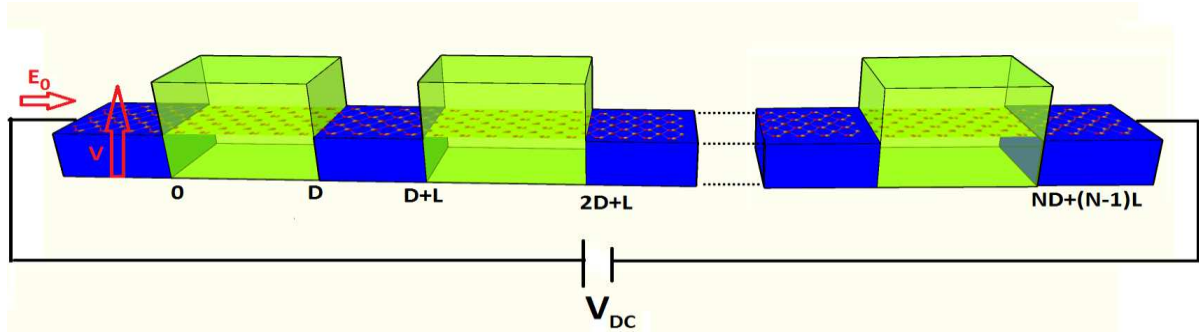


Fig 1. A schematic view of monolayer phosphorene superlattice with N barriers of width D . L is the width of the separation of the barriers.

3. Results and discussion

In this part, the probability of transmission for the single-layer phosphorene superlattice is investigated in terms of different physical factors including the landing energy, obstacle width, number of obstacles, incident angle, and distance between two obstacles by the method explained in the previous part. Here, the total length of the set is smaller than the coherence length that has been got as much as 273 nm by applying relation $l = h/2e \mu \sqrt{(ne/\pi)}$ [50,51] and substituting the associated values [29,52,53]. The parameters of e , n_e , μ , and h in this relation are electron charge, carrier density, charge carrier mobility and Planck's constant, respectively. Furthermore, The width of the barrier has not taken less than 1nm, because the lattice periodicity is 4.43\AA [10]. Initially, to study the influence of obstacles number and incident energy on the angular transmission probability, the angular transmission probability in term of incoming energy is depicted in Fig.2 for one, twenty and, fifty barriers. It is observed that for a single obstacle, the transmission probability does not reach 1 for all incoming energies at the zero-incident angle as has been demonstrated in the other works [1,39,41,42]. Increasing the barrier number to twenty barriers, a full transmission probability has been observed for incident energies of less than 2 eV and greater than 1.7eV however in the presence of Rashba effect, the full transmission probability for incoming energy of 2.5eV

has been observed in five barriers[54]. There is also the full transmission possibility at non-zero angles for twenty barriers in energies above the barrier height while there isn't for the incoming angles of zero. Incrementing the obstacle number to fifty, the full transmission probability did not occur in zero incoming angles for incident energies below the barrier height while a full transmission probability was observed for the incoming energy larger than 3.2eV and less than 3.5eV. It is generally recognized from this figure, that a full transmission probability for the incident angles of zero occurs at twenty obstacles for a barrier width of 1nm and the distance between two barriers of 1 nm. This feature can be exerted in the layout of the electronic devices.

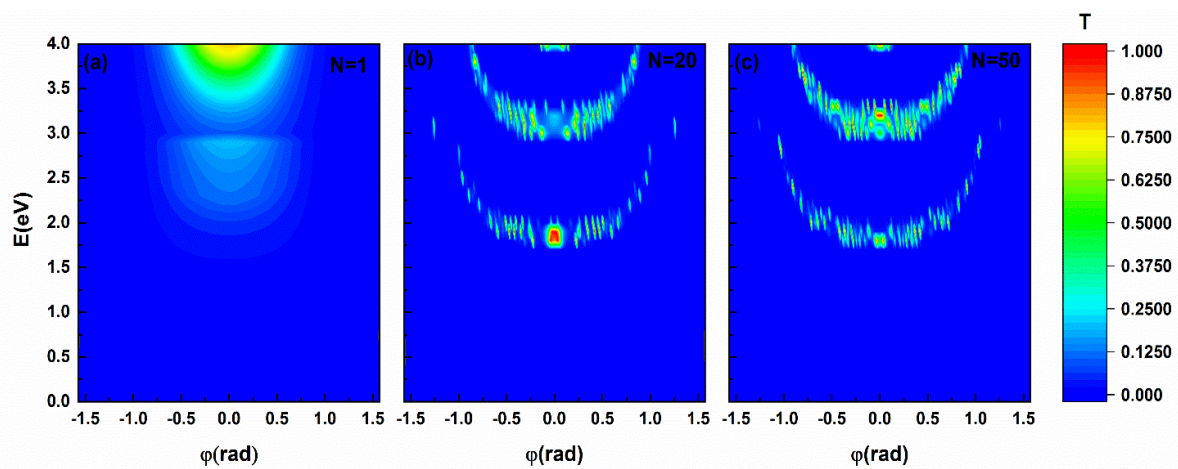


Fig 2. The transmission probability versus incoming angle and incoming energy for (a) single, (b) twenty, and (c) fifty obstacles, respectively. In shape, the thickness of the barrier and its height, and the distance between the two barriers are $D=1$ nm, $V_0=3$ eV, $L=1$ nm, respectively.

In continuation, to further study the influence of the incoming energy on the transmission probability, we plotted it versus incoming energy for the zero-landing angle in Fig. 3 for one, five, ten, and twenty barriers for different barrier widths. It is clear cut that full transmission probability for a single barrier has not occurred in energies less than the obstacle height for any of the obstacle widths as has been demonstrated in the other works [1,39,41,42]. The transmission probability of 0.93, which is the maximum transmission probability for a single barrier, occurred at $D = 2$ nm for the incident energy of 2.8eV. As well, the full transmission probability for a single barrier has not happened for incoming energy greater than the obstacle height as has been demonstrated in the other works [1,39,41,42]. Adding the number of obstacles to five, the transmission probability of 0.98 in $D = 1$ nm has observed for incident energy of 1.8eV, while the maximum transmission probability in $D = 2$ nm has occurred in 0.97 for incident energy of 2.8eV, as well as, the highest transmission probability of 0.83 in

$D = 5\text{nm}$ has happened for incoming energy of 2.9eV . Also, the full transmission probability has observed for energies greater than the barrier height in $D = 2\text{nm}$ for incident energy of 4.7eV . Increasing the number of obstacles to ten, it has found a transmission probability of 0.95 for $D = 1\text{nm}$ in incident energy of 1.8eV , while it has happened by 0.97 in $D = 2\text{nm}$ for incoming energy of 2.7eV , as well as a full transmission probability for incoming energy of 4.7eV , has occurred in $D = 2\text{nm}$. Moreover, the transmission probability of 0.57 has observed for energies below the barrier height for $D = 5\text{nm}$ in incoming energy of 2.9eV . Increasing the barrier number to twenty barriers has caused the highest transmission probability of 0.99 for incoming energy of 1.9 eV in $D = 1\text{nm}$. By increasing barrier widths to 2 and 5nm , is distinguished that a highest transmission probability occurred for incident energies of 2.7 eV and 2.5eV , which is 0.9 and 0.38 , respectively. In general, it can be understood that as the obstacle number raises, the transmission probability close to one, occurs for lower incoming energies and happens in less barrier width. For example, the transmission probability close to one for twenty barriers at $D = 1\text{nm}$ in incoming energy of 1.9eV is observed, in contrast, the transmission probability near one for five barriers at $D = 2\text{nm}$ in incident energy of 2.8eV is observed.

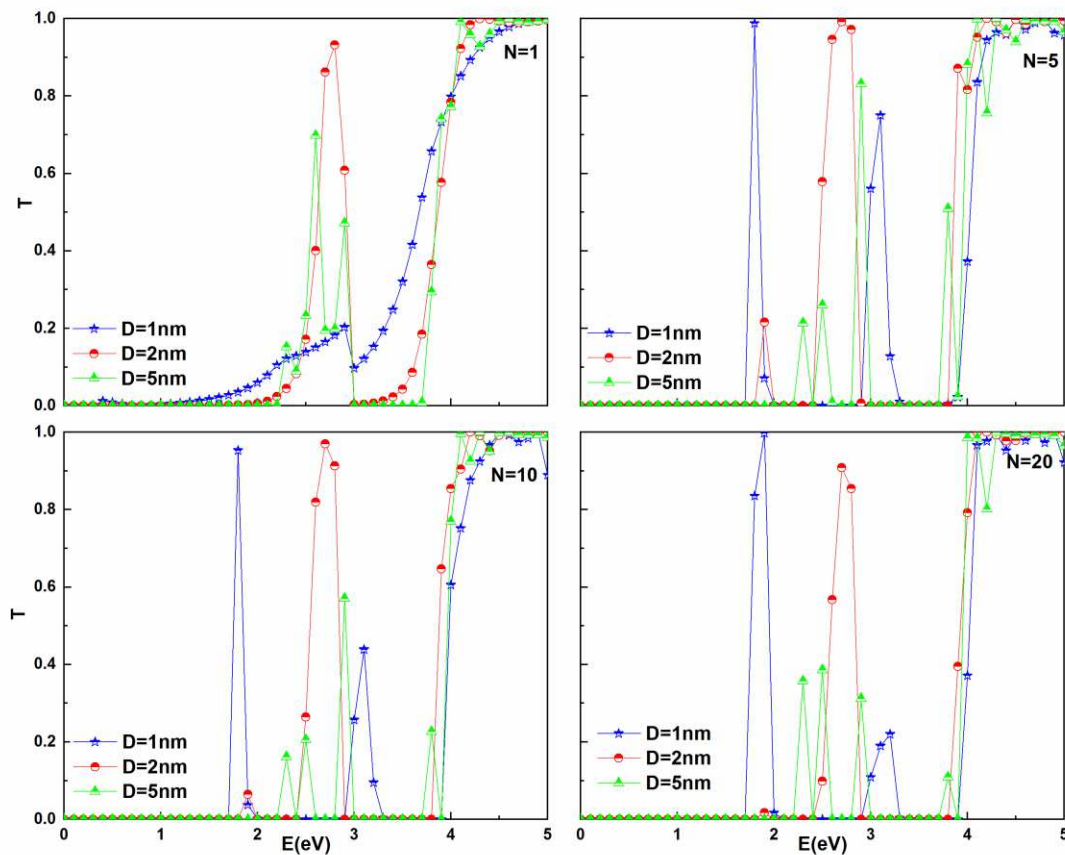


Fig 3. The transmission probability in terms of landing energy for different thickness of barrier in a zero incoming angle with the distance between the two barriers of 1nm, and the obstacle height of 3eV for one, five, ten, and twenty barriers.

In Fig. 4, the angular transmission probability is depicted for one, ten, twenty, and fifty barriers. It is clearly observed that for the one barrier at all incident angles, the transmission probability is very low. By adding the obstacle number to ten, a transmission probability is close to one in the non-zero-incident angle while it is very low for the zero-incident angles. Furthermore, it is understood that the transmission probability in the twenty barriers is 0.997 for the zero incident angles which are consistent with the results of figures 2 and 3. On the other hand, the transmission probability is greatly reduced in the zero landing angles by the increasing number of obstacles to fifty. Further, it can be discerned that a full transmission probability for the zero landing angles occurred for incident energy of 1.9eV in twenty obstacles and are consistent with the results of figures 2 and 3.

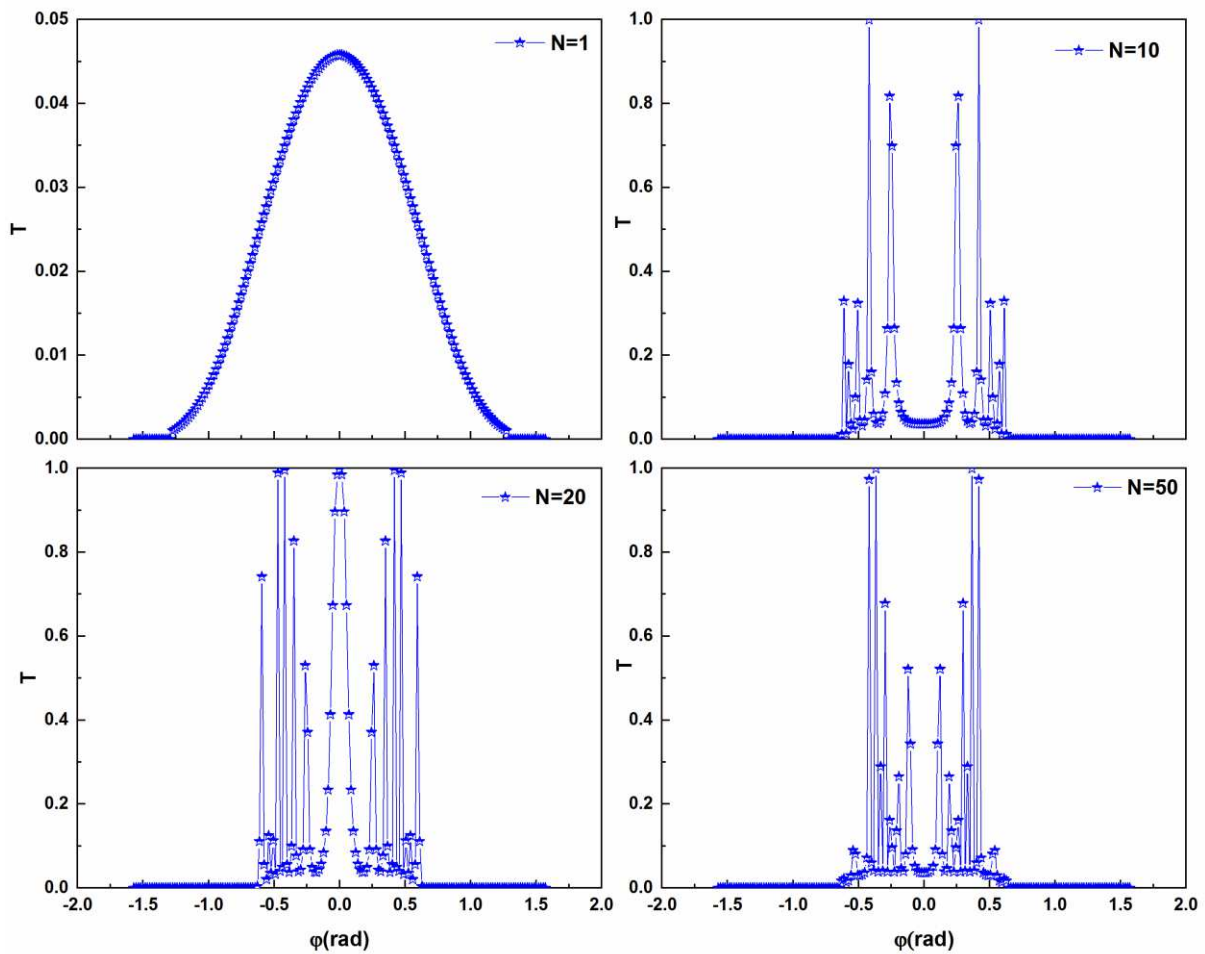


Fig 4. The probability of transmission in terms of landing angle for (a) one, (b) ten, (c) twenty, and (d) fifty obstacles, respectively. Here, incoming energy, the thickness of obstacle and its height, the distance between the two barriers are $E=1.9$ eV, $D=1$ nm, $V_0=3$ eV, $L=1$ nm, respectively.

In intention to simultaneously examine the obstacle width and incoming energy, the probability of transmission in the zero incoming angles for one, five, ten, twenty, fifty, and one hundred barriers at the barrier height of 3eV are plotted in terms of landing energy and obstacle width in Fig. 5. It is demonstrated that the full transmission probability can be achieved by changing the obstacle width. In addition, by increasing the incoming energy to 4eV, it is discerned that a transmission probability for all obstacle widths reaches one while by raising the obstacle number for this energy, the full transmission probability for a smaller number of barrier widths is observed. By extending the number of obstacles to five, it is perceived that a transmission probability for energies less than the obstacle height for a large number of barrier widths is 1, while there is little difference in transmission probability by raising the obstacle number to more than twenty.

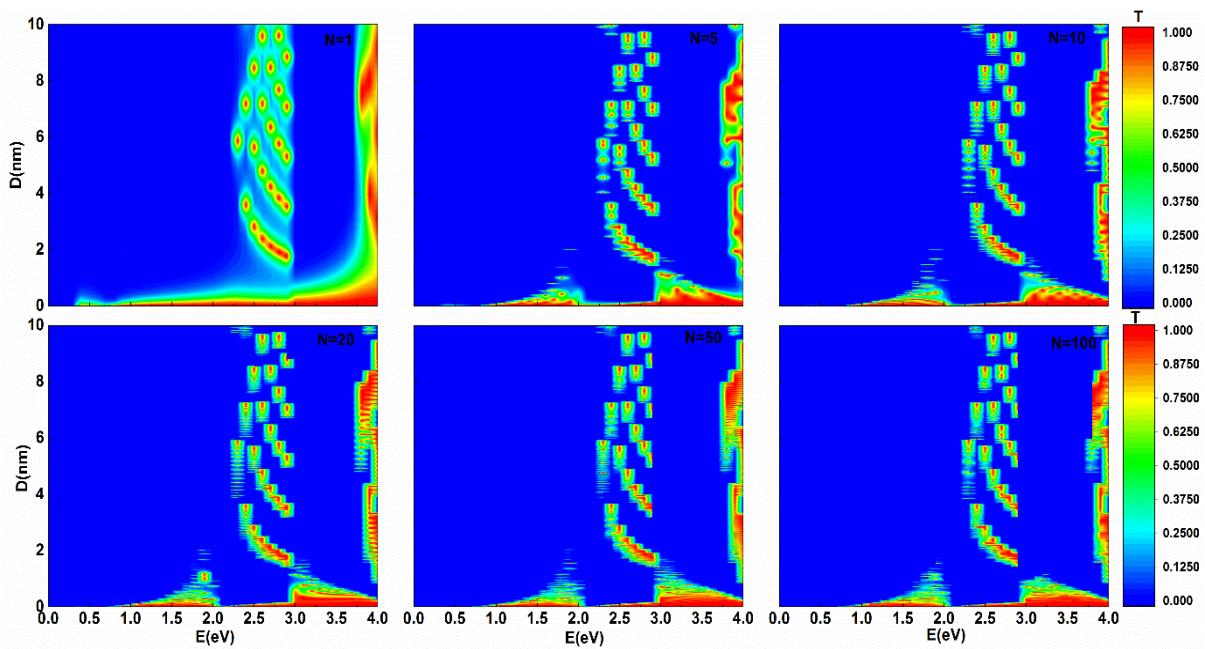


Fig 5. The transmission probability in terms of landing energy and thickness of obstacle for one, five, ten, twenty, fifty, and one hundred barriers. In the shape, the landing angle, obstacle height, and distance between the two obstacles, are $\varphi=0$, $V_0=3$ eV, $L=1$ nm, respectively.

To survey the influence of incoming energy on the transmission probability and confirming Fig. 5, the transmission probability for different energies in terms of barrier height for various barrier widths is plotted in Fig.6 for a single barrier. It is discerned that the transmission probability for the barrier height more than incident energy is very low in $D = 1$ nm, while for incident energy of 3.5eV in the height barriers of 0.4eV and 0.5eV, full transmission probability occurred in the zero-incident angle. The transmission probability close to 1 and 0.93 for $D = 2$ nm has been observed for the barrier height of 1.7 eV at the energies of 1.5 eV

and 2.5eV, respectively. As well, the transmission probability of 0.93 has been seen for incident energy of 3.5eV in the barrier height of 3.7eV at $D=2\text{nm}$. By increasing the barrier width to 5nm, it is seen that the transmission probability of one has not befallen for any of the energies less than the obstacle height. In general, it can be discerned from Fig. 6 that a full transmission probability for single barrier has occurred in $D=2\text{nm}$, which corresponds to the results of Fig. 3 and 5.

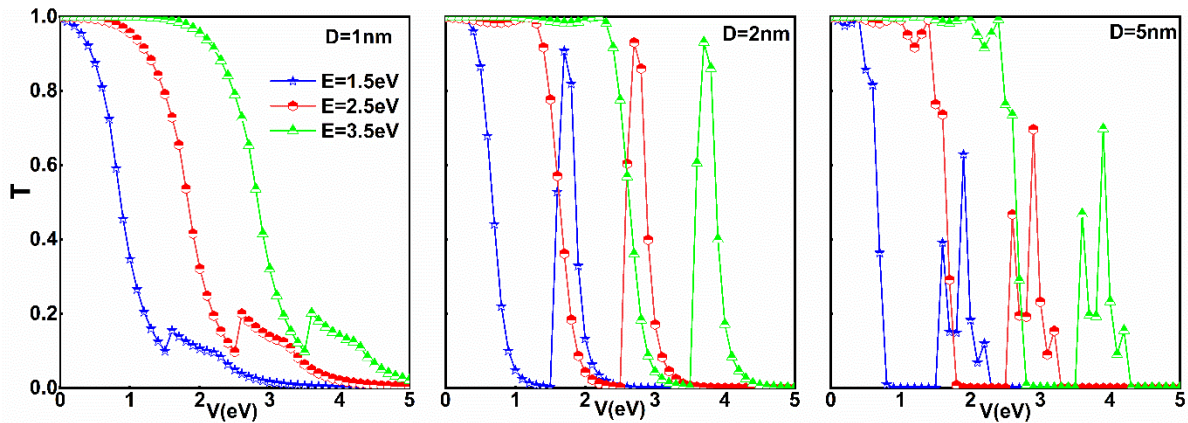


Fig 6. The transmission probability in terms of obstacle height for various incoming energies in barrier thickness of 1nm, 2nm, and 5nm for the single barrier at the zero-incoming angle.

4. Conclusions

In brief, we surveyed the transmission probability by exerting the transfer matrix method in monolayer Phosphorene superlattice. The findings demonstrate that transmission probability depends on incoming energy and the obstacle width. Increasing the obstacle number, a transmission probability close to one occurs for lower incident energies and smaller barriers width. Besides, we witnessed that the most transmission probability in the incident angle of zero that is 0.997 has occurred in twenty barriers. As well, the results have exhibited that the probability of transmission at the zero-landing angle decreased by adding the obstacle number to more than twenty barriers. In addition, a complete transmission probability has been befallen by changing the obstacle width.

Acknowledgments

This work was supported by Iran University of Science and Technology (IUST) (Grant No. 160/18402).

Orcid number: 0000-0002-9622-1232

Researcher Id: S-8830-2018

References

1. Kh, H.H., and Faizabadi, E. (2018) Dwell time, Hartman effect and transport properties in a ferromagnetic phosphorene monolayer. *J. Phys. Condens. Matter*, **30** (8), 85303.
2. Liu, H., Neal, A.T., Zhu, Z., Luo, Z., Xu, X., Tománek, D., and Ye, P.D. (2014) ACS Nano 8, 4033 (2014). *CrossRef Google Sch.*
3. Qiao, J., Kong, X., Hu, Z.-X., Yang, F., and Ji, W. (2014) High-mobility transport anisotropy and linear dichroism in few-layer black phosphorus. *Nat. Commun.*, **5**, 4475.
4. Xia, F. (2014) F. Xia, H. Wang, and Y. Jia, Nat. Commun. 5, 4458 (2014). *Nat. Commun.*, **5**, 4458.
5. Castellanos-Gomez, A. (2014) A. Castellanos-Gomez, L. Vicarelli, E. Prada, JO Island, KL Narasimha-Acharya, SI Blanter, DJ Groenendijk, M. Buscema, GA Steele, JV Alvarez, HW Zandbergen, JJ Palacios, and HSJ van der Zant, 2D Mater. 1, 025001 (2014). *2D Mater.*, **1**, 25001.
6. Ezawa, M. (2014) M. Ezawa, New J. Phys. 16, 115004 (2014). *New J. Phys.*, **16**, 115004.
7. Zhou, X.Y. (2015) XY Zhou, R. Zhang, JP Sun, YL Zou, D. Zhang, WK Lou, F. Cheng, GH Zhou, F. Zhai, and K. Chang, Sci. Rep. 5, 12295 (2015). *Sci. Rep.*, **5**, 12295.
8. Buscema, M., Groenendijk, D.J., Blanter, S.I., Steele, G.A., Van Der Zant, H.S.J., and Castellanos-Gomez, A. (2014) Fast and broadband photoresponse of few-layer black phosphorus field-effect transistors. *Nano Lett.*, **14** (6), 3347–3352.
9. Ezawa, M. (2014) Electrically tunable conductance and edge modes in topological crystalline insulator thin films: minimal tight-binding model analysis. *New J. Phys.*, **16** (6), 65015.
10. Ezawa, M. (2014) Topological origin of quasi-flat edge band in phosphorene. *New J. Phys.*, **16** (11), 115004.
11. Koenig, S.P. (2014) SP Koenig, RA Doganov, H. Schmidt, AH Castro Neto, and B.

- Özyilmaz, *Appl. Phys. Lett.* 104, 103106 (2014). *Appl. Phys. Lett.*, **104**, 103106.
12. Rodin, A.S., Carvalho, A., and Neto, A.H.C. (2014) Strain-induced gap modification in black phosphorus. *Phys. Rev. Lett.*, **112** (17), 176801.
 13. Rudenko, A.N., and Katsnelson, M.I. (2014) Quasiparticle band structure and tight-binding model for single- and bilayer black phosphorus. *Phys. Rev. B*, **89** (20), 201408.
 14. Lee, S., Yang, F., Suh, J., Yang, S., Lee, Y., Li, G., Choe, H.S., Suslu, A., Chen, Y., and Ko, C. (2015) Anisotropic in-plane thermal conductivity of black phosphorus nanoribbons at temperatures higher than 100 K. *Nat. Commun.*, **6**, 8573.
 15. Sorkin, V., Cai, Y., Ong, Z., Zhang, G., and Zhang, Y.-W. (2017) Recent advances in the study of phosphorene and its nanostructures. *Crit. Rev. Solid State Mater. Sci.*, **42** (1), 1–82.
 16. Wu, Q., Shen, L., Yang, M., Cai, Y., Huang, Z., and Feng, Y.P. (2015) Electronic and transport properties of phosphorene nanoribbons. *Phys. Rev. B*, **92** (3), 35436.
 17. Guo, H., Lu, N., Dai, J., Wu, X., and Zeng, X.C. (2014) Phosphorene nanoribbons, phosphorus nanotubes, and van der Waals multilayers. *J. Phys. Chem. C*, **118** (25), 14051–14059.
 18. Carvalho, A., Rodin, A.S., and Neto, A.H.C. (2014) Phosphorene nanoribbons. *EPL (Europhysics Lett.)*, **108** (4), 47005.
 19. Nourbakhsh, Z., and Asgari, R. (2016) Excitons and optical spectra of phosphorene nanoribbons. *Phys. Rev. B*, **94** (3), 35437.
 20. Hu, W., Lin, L., Zhang, R., Yang, C., and Yang, J. (2017) Highly efficient photocatalytic water splitting over edge-modified phosphorene nanoribbons. *J. Am. Chem. Soc.*, **139** (43), 15429–15436.
 21. Masih Das, P., Danda, G., Cupo, A., Parkin, W.M., Liang, L., Kharche, N., Ling, X., Huang, S., Dresselhaus, M.S., and Meunier, V. (2016) Controlled sculpture of black phosphorus nanoribbons. *ACS Nano*, **10** (6), 5687–5695.
 22. Yang, Y.-R., Zhang, Z.-Q., Gu, L., and Fu, H.-H. (2016) Spin-dependent Seebeck effect in zigzag black phosphorene nanoribbons. *RSC Adv.*, **6** (50), 44019–44023.
 23. Sisakht, E.T., Fazileh, F., Zare, M.H., Zarenia, M., and Peeters, F.M. (2016) Strain-induced topological phase transition in phosphorene and in phosphorene nanoribbons.

- Phys. Rev. B*, **94** (8), 85417.
24. Wu, X., Zhang, X., Wang, X., and Zeng, Z. (2016) Spin density waves predicted in zigzag puckered phosphorene, arsenene and antimonene nanoribbons. *AIP Adv.*, **6** (4), 45318.
 25. Poljak, M., and Suligoj, T. (2016) Immunity of electronic and transport properties of phosphorene nanoribbons to edge defects. *Nano Res.*, **9** (6), 1723–1734.
 26. Yang, G., Xu, S., Zhang, W., Ma, T., and Wu, C. (2016) Room-temperature magnetism on the zigzag edges of phosphorene nanoribbons. *Phys. Rev. B*, **94** (7), 75106.
 27. Zhang, J., Liu, H.J., Cheng, L., Wei, J., Liang, J.H., Fan, D.D., Shi, J., Tang, X.F., and Zhang, Q.J. (2015) Erratum: Phosphorene nanoribbon as a promising candidate for thermoelectric applications. *Sci. Rep.*, **5**.
 28. Yao, Q., Huang, C., Yuan, Y., Liu, Y., Liu, S., Deng, K., and Kan, E. (2015) Theoretical prediction of phosphorene and nanoribbons as fast-charging Li ion battery anode materials. *J. Phys. Chem. C*, **119** (12), 6923–6928.
 29. Liu, H., Neal, A.T., Zhu, Z., Luo, Z., Xu, X., Tománek, D., and Ye, P.D. (2014) Phosphorene: an unexplored 2D semiconductor with a high hole mobility. *ACS Nano*, **8** (4), 4033–4041.
 30. Zhang, S., Yang, J., Xu, R., Wang, F., Li, W., Ghufran, M., Zhang, Y.-W., Yu, Z., Zhang, G., and Qin, Q. (2014) Extraordinary photoluminescence and strong temperature/angle-dependent Raman responses in few-layer phosphorene. *ACS Nano*, **8** (9), 9590–9596.
 31. Li, L., Kim, J., Jin, C., Ye, G.J., Qiu, D.Y., Felipe, H., Shi, Z., Chen, L., Zhang, Z., and Yang, F. (2017) Direct observation of the layer-dependent electronic structure in phosphorene. *Nat. Nanotechnol.*, **12** (1), 21.
 32. Wang, X., Jones, A.M., Seyler, K.L., Tran, V., Jia, Y., Zhao, H., Wang, H., Yang, L., Xu, X., and Xia, F. (2015) Highly anisotropic and robust excitons in monolayer black phosphorus. *Nat. Nanotechnol.*, **10** (6), 517.
 33. Tran, V., Soklaski, R., Liang, Y., and Yang, L. (2014) Layer-controlled band gap and anisotropic excitons in few-layer black phosphorus. *Phys. Rev. B*, **89** (23), 235319.

34. Tran, V., Fei, R., and Yang, L. (2015) Quasiparticle energies, excitons, and optical spectra of few-layer black phosphorus. *2D Mater.*, **2** (4), 44014.
35. Rodin, A.S., Carvalho, A., and Neto, A.H.C. (2014) Excitons in anisotropic two-dimensional semiconducting crystals. *Phys. Rev. B*, **90** (7), 75429.
36. Castellanos-Gomez, A., Vicarelli, L., Prada, E., Island, J.O., Narasimha-Acharya, K.L., Blanter, S.I., Groenendijk, D.J., Buscema, M., Steele, G.A., and Alvarez, J. V (2014) Isolation and characterization of few-layer black phosphorus. *2D Mater.*, **1** (2), 25001.
37. Reich, E.S. (2014) Phosphorene excites materials scientists: physicists look past graphene for atom-thick layers that could be switches in circuits. *Nature*, **505** (7486), 19–20.
38. Kou, L., Chen, C., and Smith, S.C. (2015) Phosphorene: fabrication, properties, and applications. *J. Phys. Chem. Lett.*, **6** (14), 2794–2805.
39. Li, Z., Cao, T., Wu, M., and Louie, S.G. (2017) Generation of anisotropic massless Dirac fermions and asymmetric Klein tunneling in few-layer black phosphorus superlattices. *Nano Lett.*, **17** (4), 2280–2286.
40. Ivriq, N.R., Kordbacheh, A.A., and Kheirabadi, M.K. (2019) Quantum conductance of defected phosphorene and germanene nanoribbons. *J. Nanoparticle Res.*, **21** (11), 225.
41. Cheng, F., and He, B. (2016) Anisotropic Ballistic Transport through a Potential Barrier on Monolayer Phosphorene. *Chinese Phys. Lett.*, **33** (5), 57301.
42. De Sarkar, S., Agarwal, A., and Sengupta, K. (2017) Anisotropic transport of normal metal-barrier-normal metal junctions in monolayer phosphorene. *J. Phys. Condens. Matter*, **29** (28), 285601.
43. Popović, Z.S., Kurdestany, J.M., and Satpathy, S. (2015) Electronic structure and anisotropic Rashba spin-orbit coupling in monolayer black phosphorus. *Phys. Rev. B*, **92** (3), 35135.
44. Xu, X.G., and Cao, J.C. (2012) Dwell time in one-dimensional graphene asymmetrical barrier. *Phys. B Condens. Matter*, **407** (3), 281–285.
45. Sattari, F., and Faizabadi, E. (2013) Transport in magnetic graphene superlattice with Rashba spin-orbit interaction. *Eur. Phys. J. B*, **86** (6), 278.

46. Bai, C., Wang, J., Zhang, Y., and Yang, Y. (2011) Wavevector filtering in graphene-based double junctions with the spin-orbit interactions. *Appl. Phys. A*, **103** (2), 427–431.
47. Sattari, F., and Faizabadi, E. (2014) Spin transport and wavevector-dependent spin filtering through magnetic graphene superlattice. *Solid State Commun.*, **179**, 48–53.
48. Bercioux, D., and De Martino, A. (2010) Spin-resolved scattering through spin-orbit nanostructures in graphene. *Phys. Rev. B*, **81** (16), 165410.
49. Yokoyama, T. (2008) Controllable spin transport in ferromagnetic graphene junctions. *Phys. Rev. B*, **77** (7), 73413.
50. Banszerus, L., Schmitz, M., Engels, S., Goldsche, M., Watanabe, K., Taniguchi, T., Beschoten, B., and Stampfer, C. (2016) Ballistic transport exceeding 28 μm in CVD grown graphene. *Nano Lett.*, **16** (2), 1387–1391.
51. Farokhnezhad, M., Esmaeilzadeh, M., and Shakouri, K. (2017) Strain-modulated anisotropy of quantum transport properties in single-layer silicene: Spin and valley filtering. *Phys. Rev. B*, **96** (20), 205416.
52. Feng, X., Huang, X., Chen, L., Tan, W.C., Wang, L., and Ang, K. (2018) High mobility anisotropic black phosphorus nanoribbon field-effect transistor. *Adv. Funct. Mater.*, **28** (28), 1801524.
53. Li, L., Yu, Y., Ye, G.J., Ge, Q., Ou, X., Wu, H., Feng, D., Chen, X.H., and Zhang, Y. (2014) Black phosphorus field-effect transistors. *Nat. Nanotechnol.*, **9** (5), 372.
54. Boroughani, A., and Faizabadi, E. Spin Polarization and Spin-Flip Through Phosphorene Superlattice. *Ann. Phys.*, 1900202.